Steplike dispersion of the intermediate-frequency Raman modes in semiconducting and metallic carbon nanotubes

C. Fantini,[1] A. Jorio,[1] M. Souza,[1] R. Saito,[2] Ge. G. Samsonidze,[3] M. S. Dresselhaus,[3] and M. A. Pimenta[1]
[1]*Departamento de Física, Universidade Federal de Minas Gerais, Belo Horizonte, MG, 30123-970, Brazil*
[2]*Department of Physics, Tohoku University and CREST JST, Aoba Sendai 980-8578, Japan*
[3]*Massachusetts Institute of Technology, Cambridge, Massachusetts 02139-4307, USA*
(Received 28 April 2005; published 22 August 2005)

Resonance Raman spectra of semiconducting and metallic single-wall carbon nanotube bundles have been investigated in the spectral range between 600 and 1100 cm^{-1}, which is associated with intermediate frequency modes. A large range of nanotube diameters corresponding to HiPco and electric-arc samples (0.7–1.8 nm), and laser excitation energies between 1.62 and 2.71 eV have been used in the measurements. A rich set of peaks is observed, some of them independent of the excitation laser energy and some exhibiting a steplike dispersive behavior. The nondispersive peaks are assigned. The model proposed by Fantini *et al.* [Phys. Rev. Lett. **93**, 087401 (2004)] to explain the steplike dispersive behavior of the intermediate frequency modes is then extended to different SWNT diameters and different E_{ii} transitions, including semiconducting and metallic SWNTs.

DOI: 10.1103/PhysRevB.72.085446 PACS number(s): 78.30.Na

I. INTRODUCTION

The one-dimensional (1D) phonon and electronic structures of single-wall carbon nanotubes (SWNTs)[1,2] have been widely investigated by resonance Raman spectroscopy.[3,4] The first-order Raman spectra of carbon nanotubes show two main features that have been extensively studied: the radial breathing mode (100–400 cm^{-1}) and the graphitelike *G*-band (1500–1600 cm^{-1}). Another well known feature which is seen within the range below 1600 cm^{-1} is the *D*-band (1200–1400 cm^{-1}), which is related to a defect-induced double-resonance mechanism.[5–7] These modes are clearly seen in Fig. 1, that shows the complete first-order Raman spectrum of carbon nanotubes.

Besides these well-studied features, there are several weak Raman features in the intermediate frequency region (between 600–1100 cm^{-1}), as can be seen in the inset to Fig. 1, where the intensity is multiplied by a factor 30. By contrast with the large number of works devoted to the study of the RBM, D, and G-band features, there is only a small number of experimental[3,8–11] and theoretical[12–15] works devoted to the study of these intermediate frequency modes (IFM). From zone-folding[14] and *ab initio*[15] calculations, some IFMs are predicted to be Raman active, and according to nonresonance bond polarization theory results, several Raman modes should be present in this frequency range for short nanotubes, i.e., nanotubes with lengths of only a small number of unit cells.[12,13] It has been shown that the finite size effects disappear for nanotubes with lengths >50 nm, and only weak features around 860 cm^{-1} are predicted to be observed for large length armchair or zigzag nanotubes.[13] However, carbon nanotubes samples generally have lengths greater than 50 nm, and several features are still observed in this frequency range, so that the relation between IFM intensities and the nanotube length still remains to be demonstrated experimentally.

Experimental results reported by Alvarez *et al.*[10] show that a dispersion in frequency for some IFMs is observed when the laser excitation energy is changed. This dispersion is positive (negative) for peaks above (below) the nondispersive peak at $\omega_{oTO} \sim 860$ cm^{-1} (where oTO stands for the out-of-plane transverse optical phonon branch in graphite, as discussed later). Recently, we showed that the dispersion of these specific IFMs is not a continuous dispersion, but the modes rather exhibit a steplike dispersive behavior, characterized by peaks at constant frequencies increasing and then decreasing in intensity when E_{laser} is changed.[11] From this observation, the origin of the IFM peaks was explained based on a process involving optical absorption/emission in the E_{33}^S and E_{44}^S energy range, mediated by two E_3 symmetry phonons, one optic and one acoustic-like phonon.

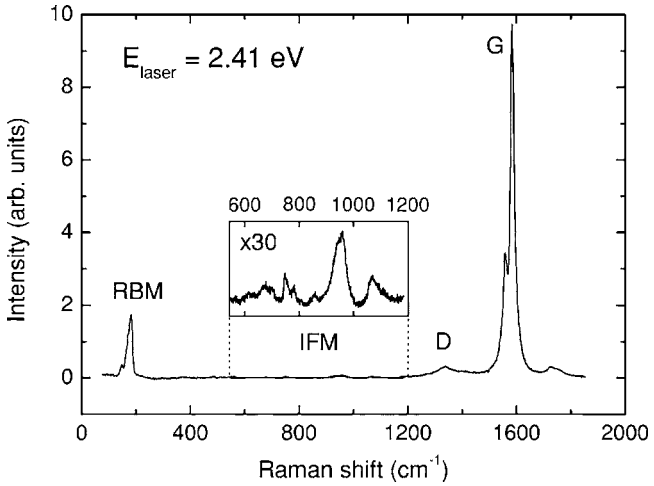

FIG. 1. Raman spectrum of SWNT bundles (electric-arc) obtained with excitation laser energy $E_{laser}=2.41$ eV. The well-studied features, namely the radial breathing mode (RBM), the disorder-induced (D) band, and the graphitelike (G) band features are assigned. The intensity for the intermediate frequency mode (IFM) region is multiplied by 30 to clearly show the richness of the low intensity IFM spectral region that is the focus of this work.

In the present work, we present an advance over findings in the previous investigation of the IFM spectra. We here extend the previous study which was developed for semiconducting nanotubes in Ref. 11 to metallic ones, with the Raman spectra taken by changing the laser excitation energy (E_{laser}) continuously. Our goal here is to generalize the model proposed in our previous work[11] for samples with different diameter distributions and in resonance with different E_{ii} optical transitions, as well as to address the origin of the nondispersive IFMs. The model is now analyzed within the extended tight-binding calculations for electronic transitions.[16–18] This model accounts for curvature effects and many-body corrections, which are important for small diameter nanotubes, and the model describes the transition energies E_{ii} within ±10 meV precision.

II. EXPERIMENTAL DETAILS

Two different kinds of SWNTs (bundles in as-prepared powder samples) were used in the experiments. Sample 1 was synthesized by an electric arc method in a 350 mbar He atmosphere using a Ni 2.1%/Co 2.1% catalyst, as studied in Ref. 11. The diameter distribution for this sample is $d_t = 1.5 \pm 0.3$ nm, as obtained by the RBM (radial breathing mode) frequency measurements. Sample 2 was synthesized by the high pressure decomposition of CO (HiPco process) and its diameter distribution is $d_t = 1.00 \pm 0.30$ nm.[19] Room temperature Raman spectra were recorded in the backscattering configuration using a Dilor *XY* triple monochromator, equipped with a cooled charge coupled device (CCD) and using several different laser line excitations from an Ar-Kr ion laser, a He-Ne laser, dye lasers with different dye solutions (Rhodamine 6G, Rhodamine 110, and DCM special), and a Ti:sapphire laser. A laser power <1 mW focused in a ~ 2 μm spot was used in the experiments. A large accumulation time (ten minutes for each data point) was needed due to the low intensity for these Raman peaks.

III. EXPERIMENTAL RESULTS

Figure 2 shows the Raman spectra of sample 1 (SWNT bundle grown by an electric arc method) obtained in the frequency range 600–1100 cm^{-1}, and measured using several laser energy (E_{laser}) values in the range 1.62–2.71 eV. The shaded areas (at about 685, 860, and 1050 cm^{-1}) show the region of the nondispersive IFMs. The arrows in Fig. 2 clearly show well-resolved IFM peaks, appearing and disappearing in the spectra as E_{laser} is varied. The same behavior is observed in the Raman spectra of a HiPco sample by changing E_{laser} in the same energy range, as shown in Fig. 3. However, we can see by the arrows in Figs. 2 and 3 that the number of IFM peaks and their frequencies are different for these two samples. For HiPco SWNTs, the nondispersive peaks are observed at about 670, 845, and 1050 cm^{-1} (shaded areas). The steplike dispersive effect is observed for four well-resolved IFM peaks below $\omega_{\text{oTO}} \sim 845$ cm^{-1}, indicated by the arrows, with frequencies at 815, 773, 725, and 670 cm^{-1}. This effect is also observed for four other IFM peaks above this frequency, appearing at 900, 930, 960, and 990 cm^{-1}.

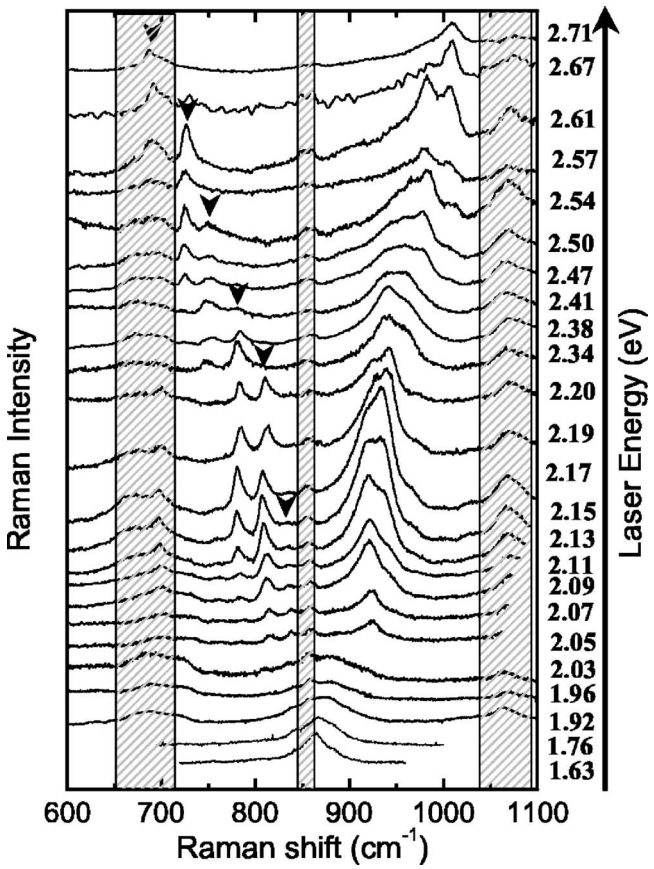

FIG. 2. Raman spectra of the IFMs for the electric-arc sample obtained by changing the laser energy between 1.63 and 2.71 eV. The arrows in the figure represent the six well-resolved and steplike dispersive IFM peaks previously observed (Ref. 11) below the first-order peak at $\omega_{\text{oTO}} \sim 860$ cm^{-1}. The shaded areas mark the nondispersive features.

Figure 4 shows a plot of E_{laser} vs ω_{IFM} for all steplike dispersive peaks shown in Figs. 2 and 3. The experimental data are represented by bars that correspond to the energy range where each peak is observed in the spectra. The black bars with diagonal lines are associated with the data of sample 1 (electric arc), and gray bars with horizontal lines are associated with sample 2 (HiPco). This figure shows that the steplike dispersive effect and the "V" shape for the steplike dispersive IFMs appear in the plot of E_{laser} vs. ω_{IFM} for both samples. The dashed and solid lines in this figure correspond to the fit of the experimental data for samples 1 and 2, respectively, obtained from the model discussed below.

IV. DISCUSSION OF THE RESULTS

A. Nondispersive IFMs

Some nondispersive modes appear in the Raman spectra of sample 1, at the frequencies $\omega_{\text{IFM}} \sim 685$, 860, and 1050 cm^{-1} and, in sample 2, at $\omega_{\text{IFM}} \sim 670$, 845, and 1050 cm^{-1}. The nondispersive peaks are observed inside the shaded regions in Figs. 2 and 3.

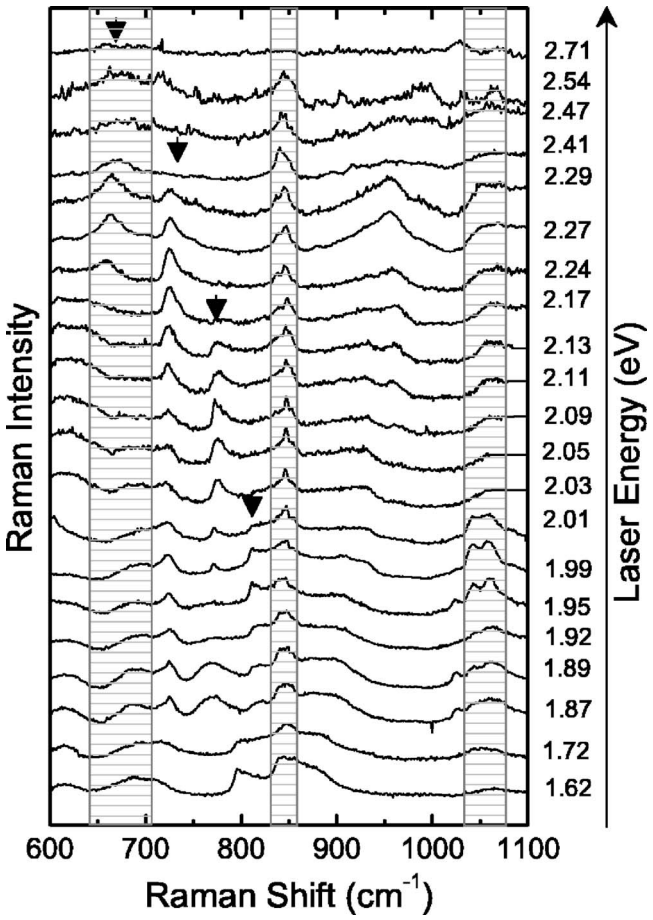

FIG. 3. Raman spectra of the IFMs for the HiPco sample obtained by changing the laser energy between 1.62 and 2.71 eV. The arrows in the figure represent the four well-resolved and steplike dispersive IFM peaks below the first-order peak at ω_{oTO} ~ 845 cm^{-1}. The shaded areas mark the nondispersive features.

The peak observed at ~ 860 (845) cm^{-1} in sample 1 (sample 2) can be assigned as a first-order Raman feature related to the oTO phonon in 2D graphite. This peak has been predicted to be Raman active by different theoretical models for infinite nanotubes,[14,15] and its predicted frequency decreases with decreasing nanotube diameter, in agreement with the observed result. Raman modes between 600–700 cm^{-1} are also predicted to be first-order Raman active,[14,15] and the nondispersive features observed in this range are also assigned to first-order Raman modes. These modes also exhibit a frequency dependence on nanotube diameter, in agreement with theory.[15] These modes can be related to the oTO and iTA phonon branches near the M point in graphite, that become Raman active in SWNTs due to zone folding. The zone folding depends also on chiral angle,[20] explaining why these features are broad. The diameter and chirality dependence also explain the changes in lineshape for these features within the same sample when E_{laser} is changed. By changing E_{laser}, SWNTs with different (d_t, θ) are resonant, leading to a slightly oscillatory behavior for the ~ 650 cm^{-1} feature, similar to observations for the D and G′ band dispersions as a function of E_{laser}.[21–23]

On the other hand, the feature observed at ~ 1050 cm^{-1} is probably not an intrinsic carbon nanotube Raman feature, but it is rather related to impurities in the samples. While the calculated phonon dispersion relations for nanotubes show a large phonon density of states in the frequency ranges 600–700 cm^{-1} and 800–900 cm^{-1}, no Raman modes are predicted in the frequency range between 1000 and 1100 cm^{-1}.[14,15] Furthermore, in contrast to the ~ 850 and ~ 650 cm^{-1} nondispersive features, the frequency observed for the ~ 1050 cm^{-1} peak is the same for the two samples, i.e., diameter independent. Finally, the ~ 1050 cm^{-1} feature is observed by infra-red absorption and its intensity decreases with annealing of the sample, and in this work, the mode is assigned to Raman peaks of C–O–C.[24]

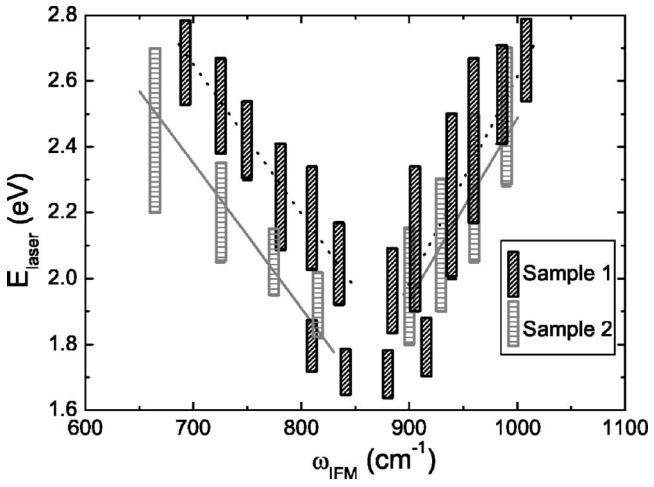

FIG. 4. E_{laser} vs ω_{IFM} for all the steplike dispersive IFM peaks observed in the two samples. The bars are the resonance energy range over which each IFM peak is observed. Black bars with diagonal lines and gray bars with horizontal lines come from arc samples and HiPco, respectively. The dashed and solid lines are the fit of the experimental data for samples 1 and 2, respectively.

B. The steplike dispersive IFMs

The positively dispersive IFMs can be fit by considering the creation of both an optic and an acousticlike phonon, and the negatively dispersive IFMs can be fit by considering the creation of an optic phonon and the annihilation of an acousticlike phonon. The equation that defines the combination modes discussed above can be written as[11]

$$\omega_{IFM}^{\pm} = \omega_{\mathcal{O}}^{\pm} \pm \omega_{\mathcal{A}}, \quad (1)$$

where $\omega_{\mathcal{O}}$ corresponds to the frequencies of the optic phonon and $\omega_{\mathcal{A}}$ is the frequency of the acousticlike phonon.[11] The frequency of the acoustic phonon can be written as $\omega_{\mathcal{A}} = v_{\mathcal{A}} q_{\perp}$ where $v_{\mathcal{A}}$ is the dispersion of the acoustic phonon, and $q_{\perp}$ is the wave vector perpendicular to the nanotube axis. Thus the experimental data are fitted by the equation

$$\omega_{IFM}^{\pm} = \omega_o^{\pm} \pm v^{\pm} q_{\perp}, \quad (2)$$

where $v^{\pm}$ considers the dispersion of the acoustic phonon plus the weak dispersion of the optic phonon. The curves in Fig. 4 were obtained considering $\omega_O^- = 1200$ cm^{-1}, $\omega_O^+ = 540$ cm^{-1}, $v^+ = 180$ cm^{-1}/eV and $v^- = 220$ cm^{-1}/eV, for

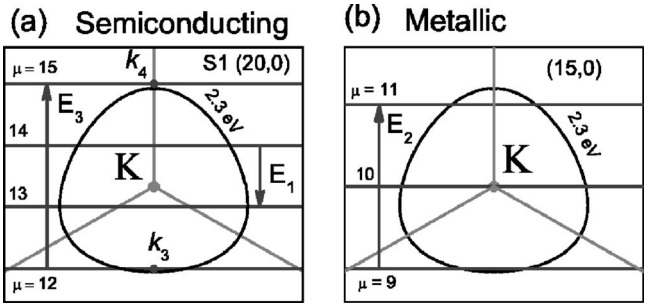

FIG. 5. Schematic picture for the allowed electronic transitions mediated by phonons for a (a) semiconducting $S1$ $(2n+m \bmod 3 = 1)$ SWNT (20,0) and (b) metallic SWNT (15,0).

sample 1, and $\omega_O^- = 1240\ \mathrm{cm}^{-1}$, $\omega_O^+ = 590\ \mathrm{cm}^{-1}$, $v^+ = 160\ \mathrm{cm}^{-1}/\mathrm{eV}$ and $v^- = 230\ \mathrm{cm}^{-1}/\mathrm{eV}$, for sample 2.

The difference between the two samples used in this work is the diameter distribution of the nanotubes in each sample. Therefore, different metallic and semiconducting SWNTs are in resonance in each case for a given E_{laser} value. Figure 5(a) shows the Brillouin zone for a semiconducting (20,0) nanotube and an equienergy contour plot at 2.3 eV. The van Hove singularities at the electronic states E_3^S and E_4^S originate from the cutting lines $\mu_3 = 12$ and $\mu_4 = 15$ at the points k_3 and k_4. According to the selection rules ($\mu_{\mathrm{phonon}} = \mu_4 - \mu_3$), the electronic states E_3^S and E_4^S must be connected by phonons with E_3 symmetry[11] as shown in Fig. 5(a). Phonons with E_3 symmetry exhibit six nodes around the nanotube circumference. The separation between two adjacent cutting lines is $2/d_t$, and therefore, for an E_3 phonon, it is possible to ascribe a wavevector perpendicular to the nanotube axis given by $q_\perp = 6/d_t$. If the spectra is obtained in a different E_{laser} range, or in a sample with a different diameter distribution, the resonances occur for different E_{ii} and $E_{i'i'}$ vHSs, and therefore phonons with different E_μ symmetry participate in the process that couples two electronic states.

Figure 5(b) shows the Brillouin zone for a metallic (15,0) nanotube and the same equi-energy contour plot at 2.3 eV. Due to the trigonal warping effect, two different van Hove singularities (E_{11}^{M-} and E_{11}^{M+}) originate from the two cutting lines ($\mu_{1-} = 9$ and $\mu_{1+} = 11$). According to the selection rules ($\mu_{\mathrm{phonon}} = \mu_{1+} - \mu_{1-}$), the IFM phonons connecting E_1^{M-} and E_1^{M+} vHSs will exhibit E_2 symmetry, as shown in Fig. 5(b). From this selection rule, the perpendicular phonon wavevector will be $q_\perp = 4/d_t$, rather than $q_\perp = 6/d_t$.

Figure 6 shows an E_{ii} vs. d_t plot in the ranges for the laser energies and sample diameters used in our experiment. This plot considers a complete (extended) tight-binding model, considering σ-π rehybridization.[16,17] The corrections due to many body effects are also included, in order to correctly reproduce the photophysics of SWNTs.[18] The solid circles represent the metallic nanotubes and the open and crossed circles represent semiconducting tubes of types S1 $(2n+m \bmod 3 = 1)$ and S2 $(2n+m \bmod 3 = 2)$, respectively. The solid lines connect the families of $2n+m$=constant, and the values of $2n+m$ are shown in the figure. The dashed and solid rectangles in this figure represent the sample diameter distributions for the electric-arc sample 1 and the HiPco sample 2, respectively.

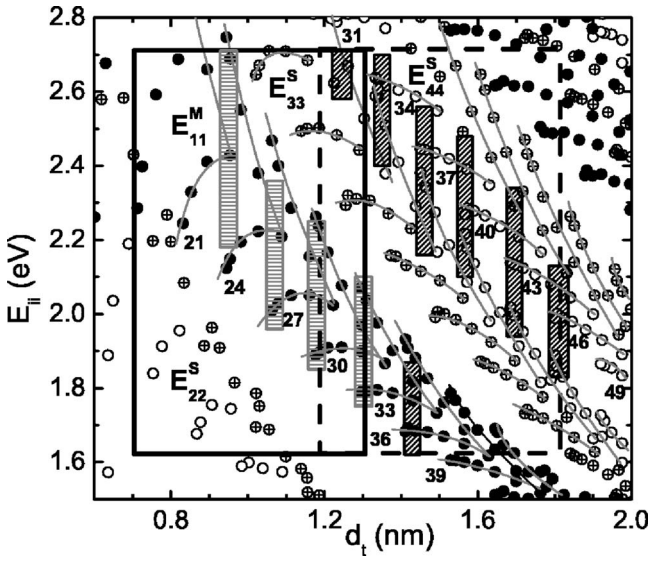

FIG. 6. Plot of the electronic transition energies (E_{ii}) vs nanotube diameter (d_t) obtained from the corrected extended tight-binding model, showing the diameter distribution for HiPco (solid rectangle) and arc electric (dashed rectangle) nanotube samples. The bars in the energy scale correspond to the energy range over which each IFM peak is in resonance, and their widths reflect the error in the d_t calculation coming from the fitting data fitting.

For sample 1, the resonance condition is mainly reached in E_{33}^S and E_{44}^S for E_{laser} values above ~ 1.9 eV, and in this case the IFMs have been explained considering the phonon coupling between the E_{33}^S and E_{44}^S transitions for SWNTs with $\theta \rightarrow 0$.[11] The six black dashed bars in Fig. 6 represent the experimental results for sample 1 corresponding to the six IFMs pointed by arrows in Fig. 2. The ω_{IFM} was changed to d_t, by applying Eq. (2) and considering $q_\perp = 6/d_t$. The $v^\pm$ values are changed from $[\mathrm{cm}^{-1}/\mathrm{eV}]$ to $[\mathrm{nmcm}^{-1}]$ by considering the approximate linear relation $E_{ii} = 2N\gamma_0 a_{\mathrm{C-C}}/d_t$ where $N = 1, 2, 3, 4, \ldots$ to E_{11}^S, E_{22}^S, E_{11}^M, $E_{33}^S, \ldots$, $\gamma_0 = 2.9$ eV, and $a_{\mathrm{C-C}} = 0.142$ nm. When $E_{\mathrm{laser}} < 1.9$ eV, the IFM peaks observed correspond to the transitions between E_1^{M-} and E_1^{M+} that are connected by E_2 phonons. By applying Eq. (2), where $q_\perp = 4/d_t$, and by considering the observed phonon frequencies, we obtain the diameter of the nanotube associated with each IFM peak.

For HiPco sample 2, the mean diameter of the nanotubes is smaller compared to the tubes in electric-arc sample 1, and the resonance condition for $E_{\mathrm{laser}} > 1.9$ eV, is also reached for metallic nanotubes. Therefore, the IFM phonons in the spectra in the visible region are related to transitions between E_1^{M-} and E_1^{M+}. We can see in Fig. 6, for HiPco nanotubes (solid rectangle), four gray dashed bars connecting E_1^{M-} and E_1^{M+}. These four bars are in agreement with the four IFM$^-$ peaks observed in Fig. 3 (see arrows). By the IFM frequencies, we can thus obtain the diameter of the SWNTs associated with each IFM feature, and thus obtain the vertical bars in Fig. 6. The diameters are obtained by Eq. (2), considering that the transitions are coupled by E_2 phonons, so that $q_\perp = 4/d_t$. Therefore, the proposed model to explain the IFM in semiconducting nanotubes[11] is here applied to explain the electronic transitions associated with metallic nanotubes.

Again, we obtain one IFM feature for each family of $(2n+m)$=constant SWNTs associated with SWNTs with $\theta \rightarrow 0$.

V. SUMMARY

The frequencies of the first-order non-dispersive mode that appear in the spectra at $\omega_{\mathrm{IFM}} \sim 650-720\ \mathrm{cm}^{-1}$ and $\sim 840-880\ \mathrm{cm}^{-1}$ increase by increasing the nanotube diameter. This diameter dependence of the mode frequencies is in agreement with theoretical predictions previously reported,[14,15] and with experimental results for other first-order Raman features in SWNTs.[25]

The model based on a second-order process involving a combination between an optic and an acousticlike phonon, previously proposed to explain the steplike dispersive modes in the Raman spectra of carbon nanotubes,[11] has been here generalized to a broad diameter range and different E_{ii}, including metallic nanotubes. We have observed here transitions between E_1^{M+} and E_1^{M-} states connected by E_2 symmetry phonons.

The results obtained for metallic nanotubes are consistent with those obtained for semiconducting tubes, where one IFM feature is observed for each $(2n+m)$=constant family. For a more complete understanding of this experimental result and the fitting parameters for the ω_{IFM} and d_t parameters, precise phonon calculations are needed for the correct identification of the optic and acousticlike phonons that participate in the process.

ACKNOWLEDGMENTS

We thank Professor L. O. Ladeira who provided us the electric arc SWNT sample. The Brazilian authors acknowledge financial support from the Instituto de Nanosciências-CNPq, and CAPES; R. S. acknowledges MEXT Grant No. 16076201; and the MIT authors acknowledge NSF DMR-04-05538.

[1] R. Saito, G. Dresselhaus, and M. S. Dresselhaus, *Physical Properties of Carbon Nanotubes* (Imperial College Press, London, 1998).

[2] S. Reich, C. Thomsen, and J. Maultzsch, *Carbon Nanotubes, Basic Concepts and Physical Properties* (Wiley-VCH, New York, 2004).

[3] A. M. Rao, E. Richter, S. Bandow, B. Chase, P. C. Eklund, R. E. Smalley, G. Dresselhaus, and M. S. Dresselhaus, Science **275**, 187 (1997).

[4] M. A. Pimenta, A. Marucci, S. A. Empedocles, M. G. Bawendi, E. B. Hanlon, A. M. Rao, P. C. Eklund, R. E. Smalley, G. Dresselhaus, and M. S. Dresselhaus, Phys. Rev. B **58**, R16016 (1998).

[5] C. Thomsen and S. Reich, Phys. Rev. Lett. **85**, 5214 (2000).

[6] R. Saito, A. Jorio, A. G. Souza Filho, G. Dresselhaus, M. S. Dresselhaus, and M. A. Pimenta, Phys. Rev. Lett. **88**, 027401 (2002).

[7] R. Saito, A. Grüneis, Ge. G. Samsonidze, V. W. Brar, G. Dresselhaus, M. S. Dresselhaus, A. Jorio, L. G. Cançado, C. Fantini, M. A. Pimenta, and A. G. Souza Filho, New J. Phys. **5**, 157 (2003).

[8] M. L. Chapelle, S. Lefrant, C. Journet, W. Maser, P. Bernier, and A. Loiseau, Carbon **98**, 705 (1998).

[9] E. Anglaret, N. Bandiab, T. Guillard, C. Journet, G. Flamant, D. Laplaze, P. Bernier, and J. L. Sauvajol, Carbon **36**, 1815 (1998).

[10] L. Alvarez, A. Righi, S. Rols, E. Anglaret, and J. L. Sauvajol, Chem. Phys. Lett. **320**, 441 (2000).

[11] C. Fantini, A. Jorio, M. Souza, L. O. Ladeira, A. G. Souza Filho, R. Saito, Ge. G. Samsonidze, G. Dresselhaus, M. S. Dresselhaus, and M. A. Pimenta, Phys. Rev. Lett. **93**, 087401 (2004).

[12] R. Saito, T. Takeya, T. Kimura, G. Dresselhaus, and M. S. Dresselhaus, Phys. Rev. B **59**, 2388 (1999).

[13] A. Rahmani, J.-L. Sauvajol, S. Rols, and C. Benoit, Phys. Rev. B **66**, 125404 (2002).

[14] P. C. Eklund, J. M. Holden, and R. A. Jishi, Carbon **33**, 959 (1995).

[15] O. Dubay and G. Kresse, Phys. Rev. B **67**, 035401 (2003).

[16] V. N. Popov, New J. Phys. **6**, 17 (2004).

[17] Ge. G. Samsonidze, R. Saito, N. Kobayashi, A. Grüneis, J. Jiang, A. Jorio, S. G. Chou, G. Dresselhaus, and M. S. Dresselhaus, Appl. Phys. Lett. **85**, 5703 (2004).

[18] A. Jorio, C. Fantini, M. A. Pimenta, R. B. Capaz, Ge. G. Samsonidze, G. Dresselhaus, M. S. Dresselhaus, J. Jiang, N. Kobayashi, A. Grüneis, and R. Saito, Phys. Rev. B **71**, 075401 (2005).

[19] P. Nikolaev, M. J. Bronikowski, R. K. Bradley, F. Rohmund, D. T. Colbert, K. A. Smith, and R. E. Smalley, Chem. Phys. Lett. **313**, 91 (1999).

[20] Ge. G. Samsonidze, R. Saito, A. Jorio, A. G. Souza Filho, A. Grüneis, M. A. Pimenta, G. Dresselhaus, and M. S. Dresselhaus, Phys. Rev. Lett. **90**, 027403 (2003).

[21] M. A. Pimenta, E. B. Hanlon, A. Marucci, P. Corio, S. D. M. Brown, S. A. Empedocles, M. G. Bawendi, G. Dresselhaus, and M. S. Dresselhaus, Braz. J. Phys. **30**, 423 (2000).

[22] A. G. Souza Filho, A. Jorio, G. Dresselhaus, M. S. Dresselhaus, R. Saito, A. K. Swan, M. S. Ünlü, B. B. Goldberg, J. H. Hafner, C. M. Lieber, and M. A. Pimenta, Phys. Rev. B **65**, 035404 (2001).

[23] J. Kürti, V. Zólyomi, A. Grüneis, and H. Kuzmany, Phys. Rev. B **65**, 165433 (2002).

[24] U. J. Kim, X. M. Liu, C. A. Furtado, G. Chen, R. Saito, J. Jiang, M. S. Dresselhaus, and P. C. Eklund (unpublished).

[25] A. G. Souza Filho, A. Jorio, Ge. G. Samsonidze, G. Dresselhaus, M. A. Pimenta, M. S. Dresselhaus, Anna K. Swan, M. S. Unlu, B. B. Goldberg, and R. Saito, Phys. Rev. B **67**, 035427 (2003).